

## ADVANCES IN THE PHYSICAL UNDERSTANDING OF LASER SURGERY AT 6.45 MICRONS

M. Shane Hutson<sup>\*</sup>, Department of Physics & Astronomy, Vanderbilt University,  
Nashville, TN 37235, USA

Glenn S. Edwards, Free Electron Laser Laboratory and Department of Physics, Duke University,  
Durham, NC 27708, USA

### Abstract

We previously presented a model that attributes the wavelength-dependence of FEL tissue ablation to partitioning of absorbed energy between protein and saline. This energy-partitioning subsequently influences the competition between protein denaturation and saline vaporization. The original model approximated cornea as a laminar material with a 50:50 saline-to-protein volume ratio. We have now refined the microscopic geometry of the model in two ways: (1) cornea is represented as a saline bath interpenetrated by a hexagonal array of protein fibrils; (2) the volume ratio is matched to the measured value, 85:15. With this volume fraction, the specific absorption coefficient for protein is much larger than previously reported. Thus, the fibril array model magnifies the differences between wavelengths that target saline versus protein. We will discuss: (1) the consistency of this model with previous, seemingly conflicting, experimental data; (2) predictions of the model, with a particular emphasis on the role of laser intensity; and (3) the experiments needed to test these predictions.

### INTRODUCTION

Early on in the development of surgical applications for free-electron lasers (FELs), the tunability of FELs was exploited to investigate the wavelength-dependence of tissue removal [1]. In the mid-IR, wavelengths near 6.45  $\mu\text{m}$  proved remarkably adept at removing defined volumes of soft tissue with very little collateral damage. In fact, tuned to this wavelength, the Vanderbilt Mark-III FEL has been used successfully in both neurological and ophthalmic surgeries on human patients [2-4]. However, due to cost and size constraints, it seems unlikely that such FELs will ever find widespread use in patient care. We now face the challenge of translating the surgical successes of mid-IR FELs to cost-effective, compact, and dedicated medical laser systems.

Several 6.45- $\mu\text{m}$  sources have already been evaluated, including a Sr vapor laser and a picosecond OPA system [5-6]. Unfortunately, the surgical performance of both sources was unacceptable. These failures highlight a key point: *the surgical performance of a laser system is not determined by wavelength alone, but by a combination of wavelength, intensity and pulse structure*. If a tabletop system matched the Mark-III FEL in all these characteristics, then one could be reasonably assured of its success. Unfortunately, such an exact match is unlikely

given the complex pulse structure of a Mark-III FEL (i.e. 2-6  $\mu\text{s}$  long superpulses, repeated at 1-30 Hz, with each superpulse containing a 2.856 GHz train of picosecond pulses) [7]. Guidance on how to relax these pulse constraints has and will come from a better understanding of the dynamics governing mid-IR tissue ablation.

It should be noted that 6.45  $\mu\text{m}$  is not an obvious choice for FEL tissue ablation. Soft tissues absorb mid-infrared light most strongly at the water absorption bands of 3.0 and 6.1  $\mu\text{m}$ ; however, wavelengths near 6.45  $\mu\text{m}$  were superior for surgical applications [1-4]. This anomalous wavelength-dependence was attributed to partitioning of the absorbed energy between the aqueous components of a tissue and its protein matrix. Thermodynamic arguments suggested that wavelengths targeting the protein matrix (like 6.45  $\mu\text{m}$ ) could reduce collateral damage [1]. Subsequently, we reported a dynamic model that confirms the plausibility of this argument [8]. The dynamic model attributes the observed wavelength-dependence to the influence of energy-partitioning and nanoscale thermal diffusion on two competing thermal processes: protein denaturation and explosive vaporization of saline.

This dynamic model has also been used to investigate the role of FEL pulse structure. As a photothermal model, it suggested that the characteristics of FEL tissue ablation should not depend on high peak intensity in an FEL's picosecond pulses [8]. Pulse-broadening experiments have recently confirmed that expanding the picosecond pulses to widths in excess of 100 ps has little effect on the ablation threshold and efficiency [9-10].

The model instead suggested a key role for high average intensity within a superpulse. By investigating a wide range of incident intensities and pulsewidths, we delineated regions of parameter space, or "sweet spots", within which the model predicts a reduced degree of collateral damage [11]. Importantly, each of the wavelengths investigated (3.0, 6.1 and 6.45  $\mu\text{m}$ ) had such a region, but the sweet spot for 6.45  $\mu\text{m}$  was much larger and encompassed much higher intensities. In collaboration with industry (PASSAT Inc, Linthicum, MD, USA), these predictions have guided the design specifications of a new 6.45- $\mu\text{m}$  laser source (several mJ of energy in 12-15 ns pulses) [12]. This laser is currently under development.

Our previous computational investigations of FEL ablation were performed on a laminar model, in which corneal stroma was approximated as alternating, 30-nm layers of saline and protein [8,11]. Although the laminar model gets the characteristic distance for nanoscale heat

<sup>\*</sup>shane.hutson@vanderbilt.edu

diffusion correct, it underestimates the temperature rise in the protein component. This underestimate arises because the laminar model is equivalent to a tissue with a 50:50 volume ratio of saline:protein. However, the measured ratio for corneal stroma is 85:15 [13]. Thus, the light absorbed by protein is actually confined to a much smaller volume than in the laminar model, yielding higher energy densities and larger temperature rises.

Here we expand our computational efforts to investigate mid-infrared laser ablation in two important ways. First, we use a geometry that more closely approximates the heterogeneous structure of corneal stroma. Results for 6.45 and 3.0- $\mu\text{m}$  irradiation are very similar to the previous laminar model. However, results for wavelengths near 6.1  $\mu\text{m}$  are qualitatively different. Most interestingly, the sweet spot at this wavelength actually splits in two. Second, we isolate the role of energy-partitioning by investigating the five mid-infrared wavelengths for which the tissue absorption coefficient is matched to that at 6.45  $\mu\text{m}$ . The computational results from this matched set help explain previous experimental results and suggest new experiments to test the predictions of our model.

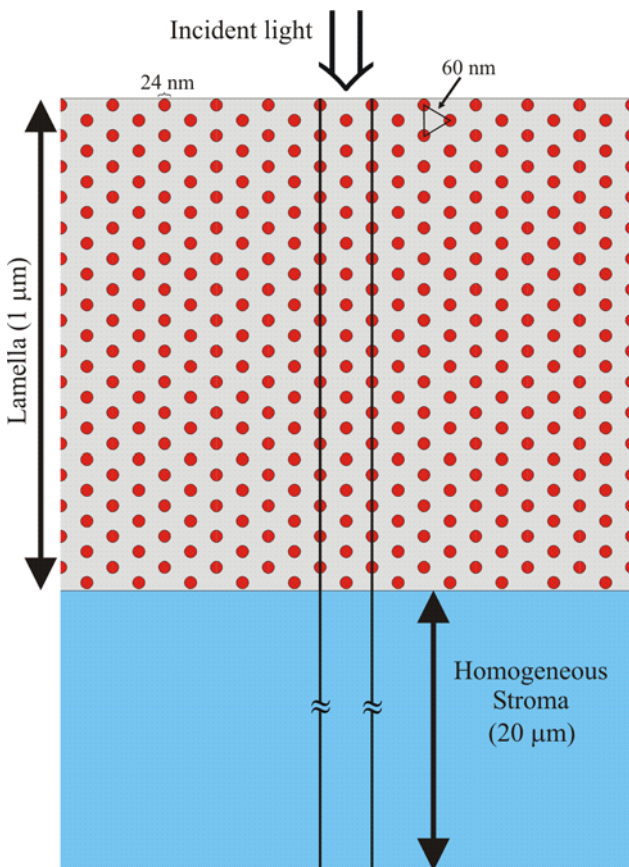


**Figure 1.** Geometry used to model laser heating in corneal stroma. The microstructure of one lamella is modeled as a hexagonal array of collagen fibrils (red) immersed in a saline bath (grey). Beyond the first lamella, the stroma is treated as a homogeneous material (blue).

## METHODS

Corneal stroma consists of hundreds of lamellae, each 1-2  $\mu\text{m}$  thick, where each lamella contains a quasi-hexagonal array of collagen fibrils [14]. The collagen fibrils within a lamella are nearly parallel, whereas those in adjacent lamellae are crossed. Based on this ultrastructure, we model corneal stroma with two layers. The first layer is a single heterogeneous lamella (1- $\mu\text{m}$  thick) composed of a hexagonal array of collagen fibrils in a saline bath. The interfibrillar spacing is 60 nm and the fibril diameter is 24 nm. These distances are consistent with cross-sectional transmission electron micrographs of stroma, [14] and yield a volume fraction ratio of 85:15. We model the remainder of stroma as a 20- $\mu\text{m}$  thick homogeneous layer. A graphical representation of this geometry is shown in Figure 1.

The symmetries and length scales of the geometry allow us to simplify the model. Since we are modeling irradiation with spot diameters of 100  $\mu\text{m}$  or more, heat diffusion in the direction parallel to the tissue surface and parallel to the fibrils is negligible for times less than  $\sim 10$  ms [15]. However, the onset of material removal in FEL ablation occurs within 10's to 100's of nanoseconds. Thus, we may reduce the geometry to a single plane. A similar argument applies to long-range heat diffusion in the direction parallel to the surface and perpendicular to the fibrils. To maintain a proper consideration of short-range heat diffusion in this direction, we (1) reduce the geometry to the width of a unit cell in the hexagonal lattice and (2) apply a zero heat flux boundary condition on the lateral edges of this section (vertical solid lines).

Laser heating and heat diffusion within this thin strip of stroma is described by Fourier's equation, [16]

$$\rho c_p \frac{\partial T}{\partial t} = \kappa \nabla^2 T + Q \quad (1)$$

where  $\rho$  is the density,  $c_p$  is the specific heat at constant pressure and  $\kappa$  is the thermal conductivity. Saline, protein and homogeneous regions are assigned specific  $\rho$ ,  $c_p$  and  $\kappa$  [13]. The heat source term,  $Q$ , represents the absorption of laser energy. A Neumann insulating boundary condition is applied to the air-tissue interface and a Dirichlet boundary condition (zero temperature rise) is applied to the rear of the homogeneous stroma layer.

To compute the specific heat source terms for each component, we measured mid-infrared spectra of porcine corneal stroma and saline. These spectra were measured in attenuated total reflectance (ATR) with a Bruker IFS-66 Fourier-Transform Infrared (FTIR) spectrometer and a single-bounce ZnSe crystal. After correction for the  $1/\lambda$  dependence of the sampling depth, the saline absorbance spectrum was interactively subtracted from the stroma absorbance spectrum to minimize the water association band centered at 4.7  $\mu\text{m}$ . The resultant spectrum represents the absorbance spectrum of the protein component of stroma. The difference between this result and the original stroma spectrum is the absorbance spectrum of the saline component.

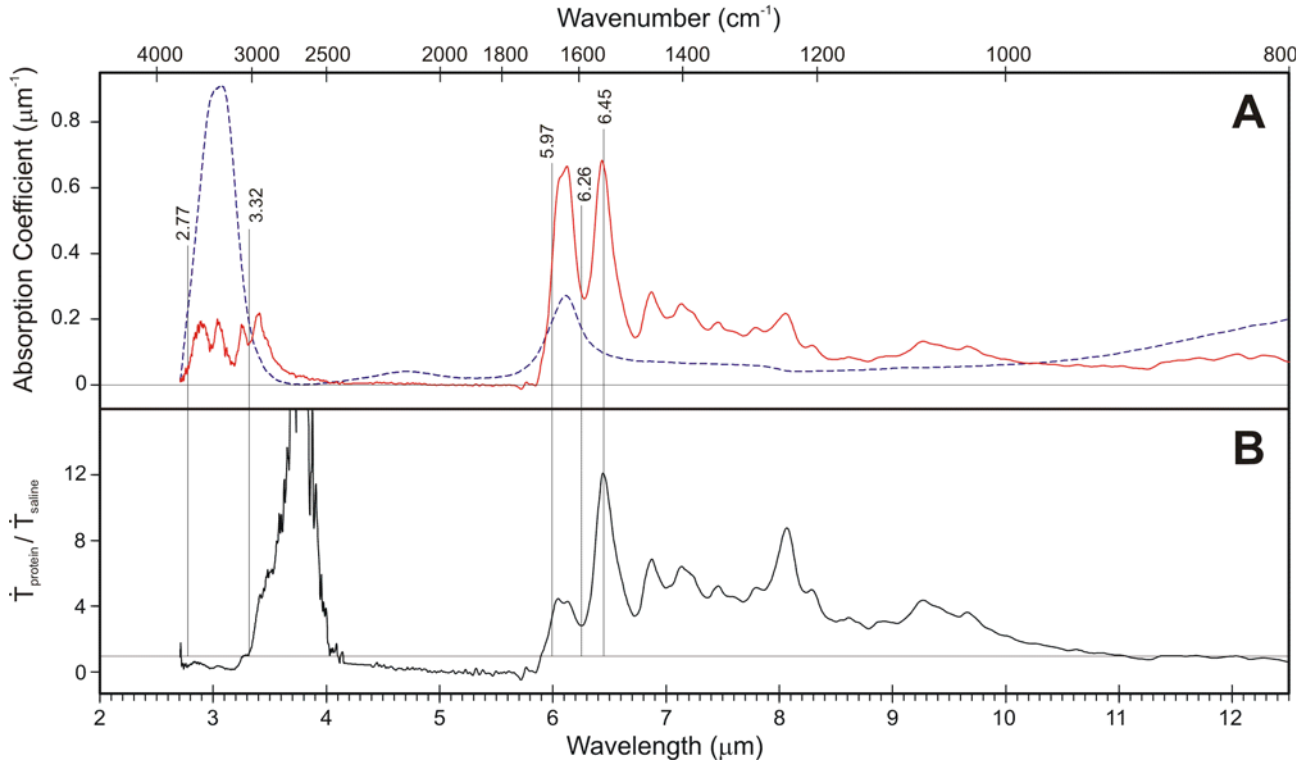


**Figure 2.** Component-specific absorption of light by the two major components of corneal stroma. **A.** Absorption coefficients for the protein (**red solid**) and saline (**blue dashed**) components based on stroma that is 85% saline by volume. The ratio of these spectra represents the relative laser energy density deposited in each. **B.** Using the respective heat capacities, one can calculate a ratio of the heating rates in the absence of heat diffusion.

A ratio of the component absorbance spectra reflects how the total incident energy is partitioned. However, for thermal modeling, we need the magnitudes of the heat sources, i.e. the deposited *energy density*. To convert the absorbance spectra,  $A$ , to the appropriate absorption coefficients,  $\alpha$ , we must consider the fraction of stromal volume,  $f_v$ , occupied by each component. Based on a stroma that is 80% water by weight and the respective densities of saline and protein, the volume fraction ratio of stroma is 85:15 (water-to-protein) [13]. Following a simple Beer-Lambert law, the absorbance of each component is related to its absorption coefficient by:

$$f_v l \alpha = A \ln 10. \quad (2)$$

The unknown sampling depth,  $l$ , is found by forcing the absorption coefficient of the 6.1- $\mu\text{m}$  saline peak to 0.27  $\mu\text{m}^{-1}$  [17]. The resulting absorption coefficients are shown in Figure 2.

The local heat source term is then given by

$$Q = (1 - R) I \alpha_i e^{-z \alpha_{\text{stroma}}} \quad (3)$$

where  $R$  is the reflection coefficient for the air-tissue interface,  $I$  is the incident intensity of the laser,  $\alpha_i$  represents the component-specific absorption coefficient, and  $z$  is depth into the tissue. Using this heat source term and the geometry described above, Fourier's equation was solved numerically on a 2D triangular mesh using a finite element model running under Matlab (The MathWorks

Inc., Natick, MA). Solutions were calculated for 181 logarithmically spaced times from  $10^{-12}$  to  $10^{-3}$  s.

From these thermal histories, the accumulated protein denaturation was calculated by integrating an Arrhenius formulation [8,13]. Explosive vaporization of saline was treated as a threshold event at the superheat limit of saline, 575 K [18]. Note that the validity of this thermal model only extends to the wavelength and intensity-dependent onset of vaporization.

## RESULTS

The component-specific absorption coefficients for corneal stroma reveal that the energy density deposited into protein exceeds that deposited into saline for a wide range of wavelengths (3.4-4 and 6-10  $\mu\text{m}$ ). This region includes the amide I, II and III, as well as the CH-stretch absorption bands of protein. Since the heat capacity of protein is less than saline, the heating rate ratio is greater than one (i.e. protein is always hotter than saline) over an even wider wavelength range. In Table 1, the penetration depths ( $1/\alpha$ ) and heating rate ratios are reported for the three strongest mid-infrared absorption bands of soft tissues (3.0, 6.1 and 6.45  $\mu\text{m}$ ). Note that these penetration depths reflect the measured volume fractions in cornea and thus differ from those reported previously [11]. Also included in Table 1 is a set of five wavelengths whose overall absorption matches that at 6.45  $\mu\text{m}$ . The heating rate ratio varies more than a factor of 40 over this set.

**Table 1.** Component-specific penetration depths of corneal stroma based on an 85:15 saline:protein volume fraction. The last two columns give the relative rates at which the energy density and temperatures of each component would rise due to laser heating (in the absence of heat diffusion).

$\lambda$ ( $\mu\text{m}$ )	Penetration Depths ( $\mu\text{m}$ )			Power Density Ratio (p:s)	Heating Rate Ratio (p:s)
	$\delta_{\text{stroma}}$	$\delta_{\text{protein}}$	$\delta_{\text{saline}}$		
2.77	5.5	30.3	4.8	0.16	0.28
3.32	5.5	8.1	5.2	0.64	1.12
5.97	5.5	4.1	5.8	1.41	2.47
6.26	5.5	3.7	6.0	1.63	2.83
6.45	5.5	1.5	10.3	6.93	12.08
12.5	5.5	14.4	5.0	0.34	0.60
3.0	1.3	8.5	1.1	0.13	0.23
6.1	3.1	1.5	3.7	2.41	4.20

We first compared laser-heating calculations with the hexagonal array and laminar models for 3.0 and 6.45  $\mu\text{m}$  [8]. For an intensity of  $7.3 \times 10^7 \text{ W/cm}^2$  (corresponding to the superpulse intensity at the center of a Gaussian beam, with a  $1/e^2$  spot radius of 50  $\mu\text{m}$ , and a picosecond pulse energy of 1  $\mu\text{J}$ ), the temperature profiles at the superheat limit differ as expected (not shown). At 3.0  $\mu\text{m}$ , the hexagonal array model predicts a protein temperature rise that still trails that of saline, but the temperature difference is smaller. At 6.45  $\mu\text{m}$ , the protein temperatures exceed those of saline by even more than in the laminar model. Both effects arise because the laminar model underestimated the temperature rise in the protein regions. The laminar model also predicted an exacerbated temperature difference between the surface layers. This surface effect is still present in the hexagonal array model, but at a slightly reduced extent. In general, for wavelengths that strongly target either saline or protein, the results of the hexagonal array and laminar models are qualitatively similar.

As a next step, we constructed “sweet spot” plots for each of the above wavelengths. These plots, shown in Figure 3, consist of three curves in the parameter space of intensity versus pulsewidth: (1 – green/dashed) the power density necessary to superheat saline, i.e. to ensure that energy deposition outpaces energy consumption from the growth of pre-existing vapor bubbles; (2 – solid/red) for a given intensity, the time required for the saline to reach the superheat limit; and (3 – dotted/blue) for a given intensity, the time required to accumulate 1% denaturation of protein. The sweet spot (yellow/shaded areas) represents the area of parameter space for which the structural integrity of protein is compromised (via 1% denaturation) before the onset of explosive vaporization. Graphically, this is any intensity for which curve 2 lies to the right of curve 3. For intensities that meet this criterion, the minimum pulsewidth lays on curve 2 and the maximum on curve 1. We expect laser ablation in this region to be more efficient and to cause less collateral damage.

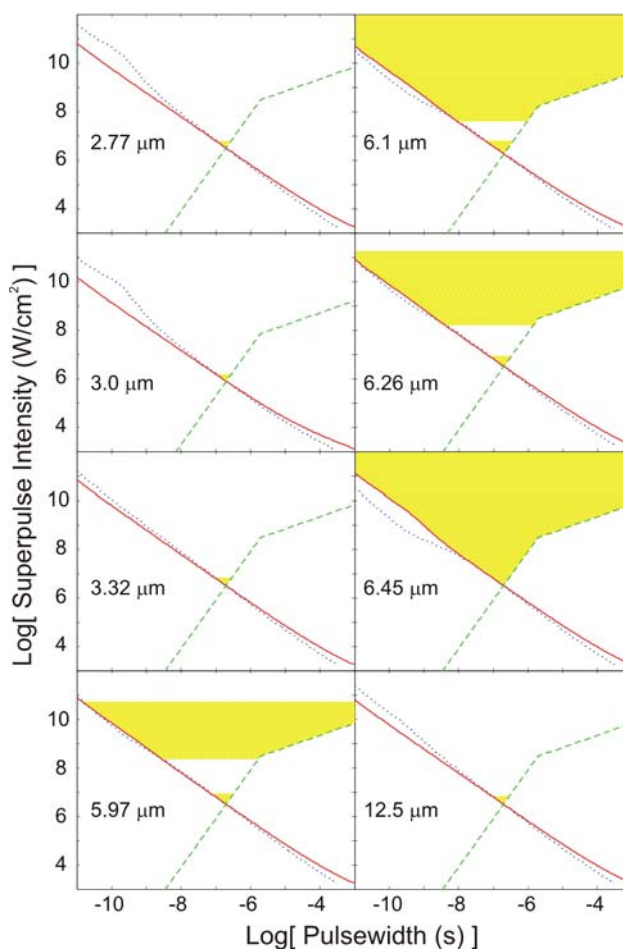


**Figure 3.** Sweet spot plots for laser ablation of corneal stroma at mid-IR wavelengths. The three curves in each plot represent the following: (**green/dashed**) power density necessary to superheat saline; (**red/solid**) combination of time and intensity required to reach the onset of explosive vaporization; (**blue/dotted**) combination of time and intensity required to accumulate 1% denaturation in the surface protein regions. The sweet spot (**shaded area**) is the set of intensities and pulsewidths for which explosive vaporization occurs after the protein matrix as been compromised by denaturation.

When compared to similar plots constructed with the laminar model [11], those for 3.0 and 6.45  $\mu\text{m}$  are similar, but the plot for 6.1  $\mu\text{m}$  is qualitatively different. Just as in the previous report, the very small sweet spot for  $\lambda= 3.0 \mu\text{m}$  stands in stark contrast to the enormous acceptable parameter range for 6.45  $\mu\text{m}$ . In fact, the upper limit of the 6.45- $\mu\text{m}$  sweet spot now lies outside the range of our model calculations. For 6.1  $\mu\text{m}$ , the sweet spot actually encompasses two regions of parameter space. In our previous laminar model calculations, the uppermost region was not included. For this wavelength, the model predicts that intensities between  $10^7$  to  $10^8 \text{ W/cm}^2$  would cause more collateral damage than either higher or lower intensities.

When we expand the calculations to include a larger set of wavelengths, we find that the sweet spot plots fall into

three classes. For wavelengths that largely target saline absorption (power density ratio less than one, e.g. 2.77, 3.0, 3.32, 12.5  $\mu\text{m}$ ), the sweet spot is very small. For wavelengths that moderately target protein (power density ratio of one to three, e.g. 5.97, 6.1, 6.26  $\mu\text{m}$ ), the sweet spot splits into a large high-intensity region and small low-intensity region that is only slightly larger than the sweet spots of saline-targeting wavelengths. Finally, if the power density ratio is very large (6.45  $\mu\text{m}$ ), the two regions merge into a single large sweet spot.

We have constructed these sweet spots on the somewhat arbitrary choice of requiring 1% denaturation to occur before the onset of vaporization. The 10% and 0.1% denaturation curves are only slightly displaced (approximately a line width) from that of 1%. However, that small difference is enough to change the constructed sweet spots. If we increased the requirement to 10%, then even 6.45  $\mu\text{m}$  would exhibit a split sweet spot. On the other hand, if we decreased the requirement to 0.1%, then the two sweet spots for 5.97, 6.1 and 6.26  $\mu\text{m}$  would merge into one.

As a more robust way to look at the interplay of protein and saline dynamics, we calculated the fractional denaturation at vaporization (FDV), i.e. the amount of denaturation accumulated in the surface protein regions when the saline reaches the superheat limit. In Figure 4A, we compare FDV versus superpulse intensity for the set of six wavelengths with matched stromal absorption coefficients. At very low intensities ( $<10^5$   $\text{W}/\text{cm}^2$ ), the laser heating process is slow enough that vaporization commences after almost all of the protein has denatured. At slightly higher intensities, FDV decreases for all six wavelengths. In this regime, the time required to reach the superheat limit decreases to less than 1  $\mu\text{s}$ , limiting the accumulation of denatured protein. All six wavelengths behave similarly because the intensity is not yet high enough to overcome nanoscale thermal diffusion. Thus, the temperature differences between protein and saline regions are negligible. This situation changes as the intensity increases further ( $>3 \times 10^6$   $\text{W}/\text{cm}^2$ ). For wavelengths that target saline, FDV continues to decline. However, for wavelengths that target protein, the trend reverses and FDV begins to increase with intensity. The minimum FDV attained in this region depends on how strongly the wavelength targets protein. The intensities are now large enough to outpace thermal diffusion and large wavelength-dependent temperature differences may arise between protein and saline regions. If the protein is substantially hotter than saline, the exponential dependence of the denaturation rate on temperature can overcome the shorter times. Finally, at very high intensities ( $>10^9$   $\text{W}/\text{cm}^2$ ), the protein-saline temperature differences have been maximized and further increases in intensity serve only to decrease the time available for denaturation. Thus, FDV again decreases with intensity. Note that this is not yet apparent for 6.45  $\mu\text{m}$  within the range of our calculations.

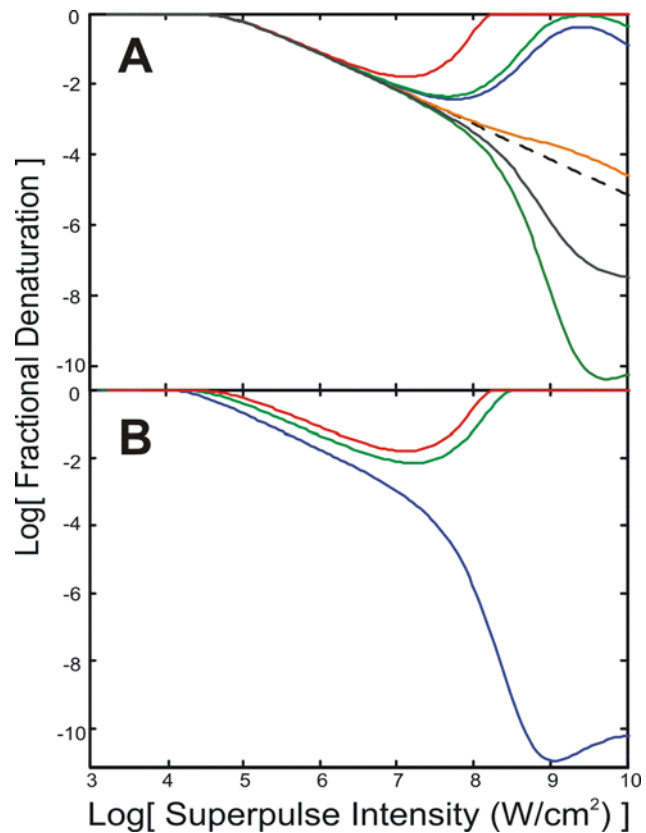


**Figure 4.** Fractional denaturation accumulated prior to vaporization in the surface protein regions. **A.** Mid-IR wavelengths with stromal absorption coefficients matched to that at 6.45  $\mu\text{m}$ . From top to bottom, the solid curves are for wavelengths of 6.45, 6.26, 5.97, 3.32, 12.5 and 2.77  $\mu\text{m}$ . The dashed curve represents a hypothetical wavelength for which there is no difference between protein and saline absorption. **B.** Peaks in the mid-IR spectra of soft tissues. From top to bottom, the curves are for 6.45, 6.1 and 3.0  $\mu\text{m}$ .

In Figure 4B, we compare FDVs for the three major mid-IR absorption peaks of soft tissues. In this case, the stromal absorption coefficients are not matched and the FDV versus intensity curves do not overlap at low intensities. For a given intensity, a larger absorption coefficient implies a faster heating rate and less time prior to vaporization. Thus the FDV curve for 3.0  $\mu\text{m}$  is always below those of 6.1 and 6.45  $\mu\text{m}$ . The curves are roughly parallel until  $\sim 3 \times 10^6$   $\text{W}/\text{cm}^2$ . They begin to diverge as the heating rate becomes sufficient to overcome nanoscale thermal conduction. At this point, FDV begins to increase with intensity for both 6.1 and 6.45  $\mu\text{m}$ . Although the very strong protein targeting of 6.45  $\mu\text{m}$  ensures that its FDV never drops below 1%, the slightly weaker targeting of 6.1  $\mu\text{m}$  allows its FDV to drop slightly below this limit.

## DISCUSSION

*Can these computational results shed light on previous experimental investigations of FEL tissue ablation? Although the original study reported an anomalous*

wavelength-dependence [1], subsequent studies found that the ablation efficiency and threshold followed the mid-IR spectra quite closely [19-20]. Interestingly, the superpulse intensities used by Edwards et al ranged from of  $4\text{-}8 \times 10^7$   $\text{W}/\text{cm}^2$  [1]. In contrast, subsequent ablation efficiency studies at FELIX and Vanderbilt were conducted between  $1\text{-}3 \times 10^6$   $\text{W}/\text{cm}^2$  [19-20]. For ablation threshold studies, the intensities are even lower (order of  $10^5$   $\text{W}/\text{cm}^2$ ) [20]. The model calculations presented here suggest that FEL ablation metrics should follow a simple wavelength-dependence, i.e. one that does not depend on the degree of protein targeting, until the superpulse intensity exceeds  $\sim 3 \times 10^6$   $\text{W}/\text{cm}^2$ . This is consistent with the available experimental results on ablation efficiency and threshold. However, there are reports of secondary ablation metrics (e.g. the size of ejected particulates in the plume) that do show a low-intensity dependence on the dominant chromophore [19]. Thus, the model presented here may explain some of the previous experimental discrepancies, but additional mechanisms must also contribute.

*What sort of experiments should tell us whether the degree of protein targeting, as modeled here, plays a significant role in the wavelength-dependence of FEL ablation?* We suggest investigations of how the ablation metrics vary with superpulse intensity. This is straightforward for ablation efficiency and collateral damage. Complementary information should be available from measurements of how the ablation threshold fluence varies with superpulse width. For such measurements on cornea, at wavelengths with matched stromal absorption, our model predicts that the thresholds should diverge below 100 ns.

*What about tissues besides cornea?* For wavelengths that strongly targeted saline or protein, the laminar and hexagonal array models agreed quite well. This agreement implies that the form factor introduced by a specific geometry is not as important as the characteristic length for nanoscale diffusion. This length scale is the key parameter for evaluating the role of energy-partitioning in other tissues. For collagenous tissues, the relevant length is the diameter of collagen fibrils. The relevant length in non-collagenous (e.g. neural) tissues is not clear.

*What do these new calculations predict for the performance of the 6.45- $\mu\text{m}$  tabletop source currently under development?* Assuming this laser will be focused to similar spot sizes as the FEL, its pulse intensity will lie in the range of  $10^9$   $\text{W}/\text{cm}^2$  [12]. According to the model calculations, this intensity is high enough to drive truly remarkable protein-saline temperature differences, yielding an FDV of order one. While the prospects for this 6.45- $\mu\text{m}$  source are very promising, we must caution that this range of intensities has not yet been explored experimentally.

Because of their wavelength-tunability and relatively long pulse length, FELs are excellent prototyping tools. FELs can be used to investigate wide swaths of parameter space to find optimal operating conditions for a specific application. The challenge, that we hope to repeatedly

face, is to then find a more economical source, dedicated to the application of interest.

## ACKNOWLEDGEMENTS

This work was supported by grants FA9550-04-1-0045 and F49620-00-1-0370 from the DOD MFEL Program.

## REFERENCES

- [1] G. Edwards, R. Logan, M. Copeland, L. Reinisch, J. Davidson, J.B. Johnson, R. Maciunas, M. Mendenhall, R. Ossoff, J. Tribble, J. Werkhaven and D. O'Day, *Nature (London)* 371 (1994) 416.
- [2] G.S. Edwards et al, *Rev. Sci. Instr.* 74 (2003) 3207.
- [3] M.L. Copeland, R.J. Maciunas and G.S. Edwards, In *Neurosurgical Topics: Advanced Techniques in Central Nervous System Metastases*, R.J. Maciunas, Ed. (The American Association of Neurological Surgeons, Park Ridge, IL, 1998), Chap. VII.
- [4] K.M. Joos, J.H. Shen, D.J. Shetlar and V.A. Cassagrande, *Lasers Surg. Med.* 27 (2000) 191.
- [5] M.A. Mackanos, E.D. Jansen, A.N. Soldatov, R.A. Haglund and B. Ivanov, *Proc. SPIE* 5319 (2004) 201.
- [6] G. Edwards, M.S. Hutson, S. Hauger, J. Kozub, J. Shen, C. Shieh, K. Topadze and K. Joos, *Proc. SPIE* 4633 (2002) 194.
- [7] J.M.J. Madey, *J. Appl. Phys.* 42 (1971) 1906.
- [8] M.S. Hutson, S.A. Hauger and G.S. Edwards, *Phys. Rev. E* 65 (2002) 061906.
- [9] M.A. Mackanos, J.A. Kozub, E.D. Jansen, *Proc. SPIE* 5319 (2004) 209.
- [10] J.A. Kozub, M.A. Mackanos, M.H. Mendenhall, E.D. Jansen, *Proc. SPIE* 5340 (2004) 87.
- [11] G.S. Edwards and M.S. Hutson, *J. Synchrotron Rad.* 10 (2003) 354.
- [12] A.I. Makarov, G.A. Pasmanik, A.A. Shilov, A.G. Spiro, L.R. Tiour and G.S. Edwards, Presented at Solid State and Diode Laser Technology Review (2004) Albuquerque, NM, USA.
- [13] J. Kampmeier, B. Radt, R. Birngruber and R. Brinkmann, *Cornea* 19 (2000) 355.
- [14] K.M. Meek and N.J. Fullwood, *Micron* 32 (2001) 261.
- [15] M.J.C. van Gemert and A.J. Welch, In *Optical-Thermal Response of Laser-Irradiated Tissue* (Plenum Press, New York, 1995), Chap. XIII.
- [16] L.D. Landau and E.M. Lifshitz, *Fluid Mechanics*, 2nd Ed. (Pergamon Press, Oxford, 1987), Chap. V.
- [17] G.M. Hale and M.R. Querry, *Appl. Opt.* 12 (1973) 555.
- [18] V.P. Skripov, *Thermophysical Properties of Liquids in the Metastable (Superheated) State* (Gordon & Breach, New York, 1988).
- [19] J.M. Auerhammer, R. Walker, A.F.G. van der Meer and B. Jean, *Appl. Phys. B* 68 (1999) 111.
- [20] S.R. Uhlhorn, Ph.D. Thesis, Vanderbilt University, April 2002.